Journal of Materials Chemistry A

ROYAL SOCIETY OF CHEMISTRY

PAPER

View Article Online
View Journal

Cite this: DOI: 10.1039/d5ta09677d

Impact of graphene quantum dot edge shapes on high-performance energy storage devices

Grainne Gilleece, *[a] Natasha Shirshova, *[a] Ensieh Hosseini,[a] Karl Coleman,[b] Marcos Perez-Pucheta[b] and Dagou Zeze[a]

Electrode materials critically influence the performance of energy storage devices such as supercapacitors and batteries. Graphene quantum dots (GQDs) are a promising material for next-generation systems due to their high surface-to-volume ratio, tunable bandgaps, and stability. Their nanoscale size creates numerous edge sites with zigzag (ZZ) or armchair (AC) configurations. Yet, the role of edge shape in electrochemical behavior remains largely unexplored. Likewise, the correlation between synthesis methods and edge configurations is unclear, hindering the development of targeted fabrication approaches. In this study, nitrogen-doped GQDs (N-GQDs) with ZZ and AC edges were synthesized *via* hydrothermal and electrochemical methods. They were subsequently characterized using physical methods (XRD, TEM, UV-Vis, Raman spectroscopy). They were then electrodeposited onto carbon fibers and their electrochemical properties were analyzed (CV, EIS). We examined the N-GQD size, edge configuration, bandgap, charge transport, and process parameters such as pH and electrolyte choice. The results show that ZZ-edged N-GQDs outperform AC-edged counterparts in capacitance (double-layer, pseudocapacitance, quantum capacitance) due to a higher density of states originating from dispersionless edge states, which are absent at AC edges. Additionally, pH variations affect ZZ N-GQDs by modulating their energy bandgap, informing electrolyte selection and material tuning to deliver target applications such as batteries or supercapacitors. This work establishes performance differences between ZZ and AC edged N-GQDs, enabling precise nanoparticle design for optimized energy storage, and opens opportunities in bandgap-engineered applications such as solar cells, LEDs, lasers, and photodetectors.

Received 26th November 2025
Accepted 12th March 2026

DOI: 10.1039/d5ta09677d

rsc.li/materials-a

Introduction

The fabrication of sustainable high-performance energy storage devices, including supercapacitors and batteries, is more important than ever amid the Global Energy Crisis. In recent years, there has been a growing interest in the development of electrochemical energy storage devices.[1] It is accepted that their performance is significantly affected by the electrode materials employed. One electrode material with great potential to improve the performance of these devices is zero-dimensional graphene quantum dots (GQDs). The benefits of integrating GQDs into supercapacitors and batteries are already well known.[2] However, optimizing the nanoparticles specifically for their use in energy storage would allow greater improvements in the devices' performance.

After synthesis of the GQDs, the edge shapes of the integrated graphene quantum dots are not commonly determined. As a result, it is not known which synthetic methods result in either zigzag or armchair edges on GQDs. This is with the exception of nanolithography where each nanoparticle is individually cut, which is extremely time-consuming and is not scalable for use in electronic devices.[3] Previous work on the variation in the bandgaps of GQDs typically focuses on the influence of nanoparticle size or doping concentration due to the straightforward controllability of these parameters.[4] However, these factors do not lead to changes in the density of states due to variations in the edge states of GQDs. These edge states will directly influence the GQDs' ability to store energy. Due to the uncertainty in synthesizing the required edge shapes, the impact of GQD edge shapes is mainly studied computationally, often without their use in energy storage devices in mind.[5] Therefore, gaining a better understanding of the influence of edge properties, both in GQDs themselves and in electrodes incorporating them, is essential for accelerating the development of high-performance energy storage devices. The work presented in this paper aims to bridge the existing knowledge gap by systematically investigating the properties of ZZ and AC edges through experimental methods. The resulting insights are then utilized to recommend tailored GQDs

[a]Department of Engineering, University of Durham, UK. E-mail: natasha.shirshova@duram.ac.uk; grainne.gilleece@durham.ac.uk
[b]Department of Chemistry, University of Liverpool, UK

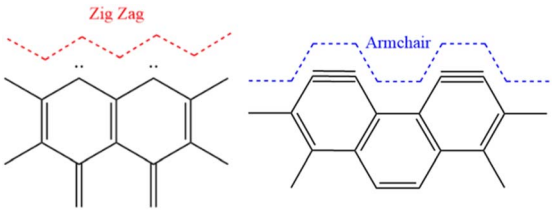

Fig. 1 Schematic representation of zigzag (left) and armchair (right) GQD edges.

expected to provide the greatest enhancement in energy-storage performance when integrated into devices.

Quantum confinement effect in GQDs

2D graphene is a zero-bandgap semimetal due to the six Dirac points in the material. The emergence of a bandgap is achieved through the quantum confinement effect in graphene quantum dots, whereby discrete energy levels form when the particle's size reaches the nanoscale. Quantum confinement effects become evident when the particle's length scale is comparable to the Bohr radius of an exciton, and the excitons are therefore confined in all three dimensions. For this reason, GQDs are known as a zero-dimensional material.[6]

Quantum confinement in GQDs is size, shape, and edge dependent.[7] Altering these parameters causes the particle's bandgap to widen or narrow, affecting its electronic properties, as a result.

GQDs can possess zigzag (ZZ) edges, armchair (AC) edges (Fig. 1), or a combination of these. ZZ edges are carbene-like, where each carbon atom at the edges of the particle contains two unshared valence electrons. In contrast, AC edges contain triple bonds between the carbon atoms at the edges of the GQD, a carbyne-like structure.[8] The bandgap on AC-edged GQDs will always be larger than that of ZZ-edged GQDs of the same size.[9]

The bandgap of GQDs changes according to the relation:

$$E_{\text{gap}} \propto \frac{1}{R} \tag{1}$$

where R is the radius of the nanoparticle. Evidently, the smaller the GQD, the larger the bandgap.

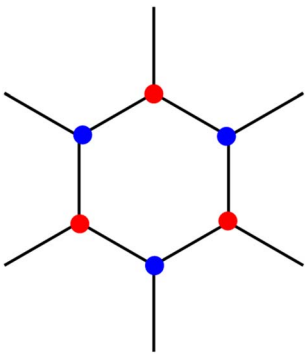

Fig. 2 Graphene lattice structure. The red and blue represent the different sublattices.

Density of states

The hexagonal structure of graphene can be thought of as two superimposed triangular sublattices (Fig. 2), which are similar by inversion symmetry.

AC and ZZ edged GQDs will display a different density of states at their Fermi level. This is a result of the sublattice geometry at their edges. The atoms at the edges of ZZ GQDs are all the same sublattice type, whereas AC GQDs terminate with an atom from each sublattice, resulting in non-identical boundary conditions describing the Hamiltonians of each edge shape. For a ZZ GQD, the wavefunction will vanish for a single sublattice at its edge, resulting in its lowest Landau level supporting two types of edge states (current carrying and dispersionless). One of these edge states (dispersionless) does not pass through the Fermi level for any non-zero doping. For AC edges the wavefunction will vanish for both sublattices and only current carrying edge states are observed. As a consequence, ZZ GQDs will always display a larger density of states at their Fermi level.[10]

Energy storage mechanisms of GQDs

Adding GQDs to energy storage devices can increase their overall storage capability.[4] GQDs store energy through two processes, namely electrical double layer capacitance, resulting from the carbon lattice, and pseudocapacitance. Oxygen-rich functional groups are introduced to GQDs synthesized from oxygen-containing precursors and are present on almost all GQDs, resulting in pseudocapacitance. The total capacitance, however, is limited by the quantum capacitance.[11]

Nanostructured materials suffer from an intrinsic limiting factor to their total capacitance, known as quantum capacitance.[11] Quantum capacitance (C_q) acts in series with traditional electrostatic capacitance according to eqn (2):

$$\frac{1}{C_{\text{total}}} = \frac{1}{C_{\text{dl}}} + \frac{1}{C_q} \tag{2}$$

where C_{total} is the total capacitance, and C_{dl} is the double layer capacitance.[11] The phenomenon results from poor screening, leading to a depolarizing field effect opposite to the dielectric polarization resulting in a reduction in field line cancellations,[12] ultimately limiting the electrode's ability to accumulate charge on its surface in response to the electrode's potential.

Graphene-based materials undergo imperfect screening due to their low density of free electrons.[13] The quantum capacitance is directly related to the material's density of states by eqn (3):

$$C_q = e\sqrt{\varepsilon\varepsilon_0 D(E_F)} \tag{3}$$

where C_q is the quantum capacitance, e, ε and ε_0 are the elementary charge, the dielectric permittivity of the material, and the vacuum permittivity, respectively, and $D(E_F)$ is the density of states.[11]

The limiting effects of quantum capacitance in GQDs can be mitigated by heteroatom doping and functionalization, as explained in the following two sections, and by introducing defects into the lattice structure.

Heteroatom doped GQDs

Carbon atoms in the GQD lattice structure can be replaced by heteroatoms (atoms other than carbon or hydrogen) through heteroatom doping, altering the structure and electronic properties of the nanoparticles. The configuration of the doped atoms, particularly whether they are doped on their basal plane or edge sites, influences the electronic properties to different extents. The doping of heteroatoms introduces defect energy levels, causing a shift in the Fermi level position and thereby altering the bandgap of the GQDs. Depending on whether the doped atoms are electron withdrawing or donating, the bandgap may be widened or narrowed by heteroatom doping.[14] Energy storage capability is typically improved upon increasing doping concentration. However, this is only up to a point since the insertion of an extremely large number of heteroatoms will compromise the inherent graphene structure. The heteroatom sites can also provide more ion diffusion channels for adsorption, alongside a higher number of active sites, improving wettability and decreasing charge transfer resistance.[15] Furthermore, heteroatom doping increases the charge-carrier density, thereby enhancing the volumetric capacity of GQDs. Higher charge carrier density also improves conductivity through faster electron transport in the nanoparticles,[16] increasing the quantum capacitance and introducing pseudocapacitance through the redox-active heteroatoms, therefore increasing the doped GQDs' specific capacitance.[17]

GQDs are most commonly doped with nitrogen, sulfur, or phosphorus. These heteroatoms have all been shown to increase the capacitance of GQDs due to the reasons outlined above, but each has its drawbacks. For instance, the extent of nitrogen doping is difficult to control, and the configuration of the doped nitrogen has a significant impact on the capacitance of the nanoparticles.[18] Phosphorus doping can broaden the electrochemical window of the electrode. However, phosphorus doping of GQDs typically reduces their conductivity due to the large atomic size of P compared to C, alongside its vacant 3d orbital. Similarly, doping GQDs with sulfur can decrease the conductivity of the nanoparticles. This results from the different bond lengths of C–S compared to C–C, which can cause a curvature in the graphene plane.[19] Since nitrogen is similar in size to carbon, it causes minimal distortion to the graphene lattice when doped into the nanoparticles. Nitrogen-doped graphene quantum dots will therefore be explored in this work.

Energy storage in functionalized GQDs

Further to edges, shape and particle size, chemical functionalization of GQDs affects quantum confinement. Functionalization occurs through covalent bonding through reactions with residual groups present on the GQDs or, more commonly, noncovalent bonding *via* hydrogen bonding, van der Waals force, π–π stacking, electrostatic interaction or chemisorption.[20] Functionalization differs from heteroatom doping since functionalized groups are not part of the GQDs lattice structure. The functionalization of GQDs can narrow their bandgap by increasing the relative nanoparticle size.

Functionalization can occur on the surface of GQDs or between the graphite layers. It can improve solvent dispersibility, shorten ion diffusion distances and increase the number of active sites present. The functional groups increase the wettability of the electrode, leading to enhanced electrolyte adsorption and promoting the formation of the electrical double-layer.[15] Furthermore, the functional groups are faradaic and lead to a pseudocapacitive contribution to the total capacitance of the GQDs.

The introduction of functional groups to edge sites of GQDs causes steric effects. When the edge sites of zigzag GQDs are passivated only by hydrogen atoms, steric effects caused by hydrogen are negligible since the carbon–carbon distance (2.46 Å) is more than double the van der Waals radius of hydrogen (1.10 Å).[21] When these hydrogen atoms are replaced by functional groups, steric hindrance begins to take place and rippling occurs at the edges of the particle, becoming more prevalent as the size of the functional group increases. The proximity of functional groups to other functional groups on the edges of the particle will evidently make a large difference to the extent of geometric changes of the GQD; the closer the functional groups are to each other, the greater the steric hindrance. The changes in planarity of the GQD affect its bandgap, decreasing its size by up to $\sim$0.3 eV.[22] The largest changes in energy gap will occur for functionalized GQDs where the functional groups are located on the GQD in such a way that molecular symmetry is preserved (*e.g.* a triangular GQD with a functional group on each corner) as these particles will retain zero energy state degeneracy of planar GQDs, while still increasing exciton localization within the structure.[23] The steric effects of functionalization of GQDs have only been studied through DFT simulations thus far and have not been investigated for synthesized GQDs with random shapes and uncontrollable locations of functional groups. For this reason, the changes in planarity of the nanoparticles due to functionalization are beyond the scope of this work and are therefore not mentioned further. As a note, while it has not been explicitly investigated in this work, armchair edge-terminated pristine GQDs likely exhibit some form of steric effect due to the sp carbon triple bond at their edges, which is shorter than the sp^2 bonds at the edges of pristine zigzag GQDs and therefore likely distorts the outermost rings to some extent.

GQDs as a supercapacitor electrode material

The presence of both electrical double layer capacitance and pseudocapacitance in GQDs contributes to a high capacitance and boosts the rate capability of the supercapacitors into which they are integrated. The GQDs regulate electrode structure during the charge/discharge process, improve kinetics, and increase electrode surface area.

GQDs have previously been investigated as an electrode material for supercapacitors in order to overcome the limitations to their energy density.[4] GQDs cannot be used alone as an electrode material due to their tendency to agglomerate, driven by their strong π–π interactions. The aggregation results in a decreased surface area, thereby reducing the electrochemically active sites of the material. Furthermore, nanoparticle size

will increase, decreasing the bandgap width. Upon excessive agglomeration, the GQDs will restack into graphene.[24] Instead, GQDs are deposited or embedded onto existing electrodes.

In all reports of GQD-enhanced supercapacitors, to the best of the authors' knowledge, the edge shapes of the GQDs used are not mentioned.[4] As discussed earlier, knowledge of the edges of GQDs used as an electrode material is extremely important to the optimization of the devices. The differences in density of states and bandgap width arising from the edge type will impact the extent to which the nanoparticles improve the device's performance.

Additionally, it has been reported that pH conditions affect quantum confinement of GQDs, with high pHs narrowing their bandgap, and low pHs widening it,[25] therefore the pH of the electrolyte in the supercapacitor must be taken into account. Reports of device fabrication in the literature do not appear to consider pH of the electrolyte, making it an important subject requiring further investigations.

Here, we aim to determine the optimal edge configurations of nitrogen-doped GQDs that yield the greatest enhancement in energy storage performance when incorporated into electrochemical energy storage systems. To this end, the synthesis of GQDs and the influence of edge structure on their surface and electrochemical characteristics are presented and examined. The changes resulting from depositing the GQDs onto carbon fiber electrodes are also reported and discussed based on detailed electrochemical characterization.

Results and discussion

Hydrothermal synthesis of N-GQDs

Nitrogen doped GQDs (N-GQDs) were synthesized in a single step process and were selected because nitrogen is more electronegative than carbon and is an electron acceptor, thereby attracting ions from the electrolyte, and improving electrochemical performance. The introduction of nitrogen *via* doping induces defect energy levels, which decreases the bandgap in GQDs. In addition to doped nitrogen, nitrogen groups can also be present on the nanoparticles as amine groups functionalized on the edges or basal plane. Further to the doped nitrogen, these amine groups will increase the specific capacitance, since they are highly ionizable and contribute to pseudocapacitive energy storage.

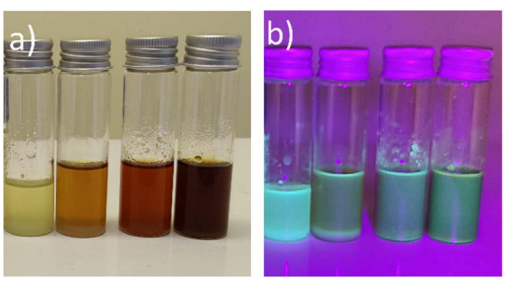

Fig. 3 HT1-4 (from left to right), corresponding to 150, 165, 180 and 195 s irradiation times, respectively; (a) under standard lighting and (b) under a 295 nm UV torch.

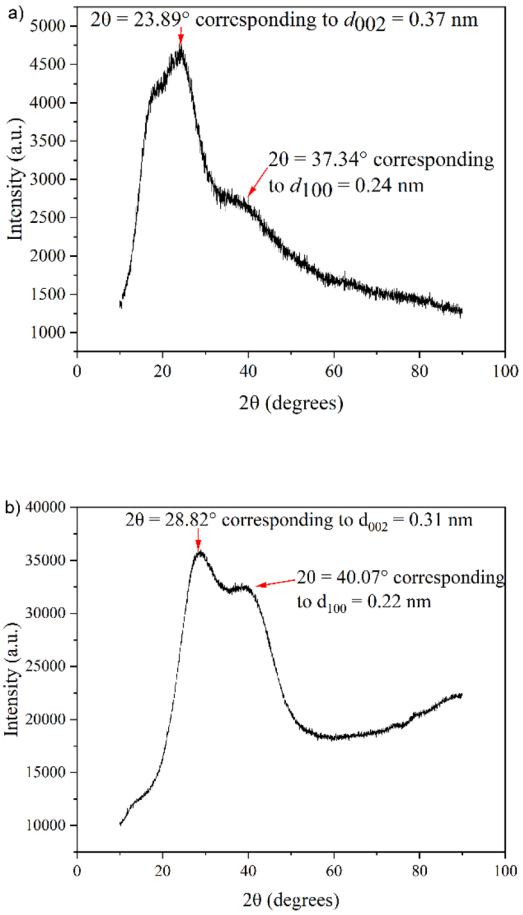

Fig. 4 XRD graph of (a) hydrothermally synthesized N-GQDs (HT1) and (b) electrochemically synthesized N-GQDs (EC1).

The microwave-assisted hydrothermal synthesis of GQDs from monosodium citrate and triethanolamine is a bottom-up synthetic technique. The rapid microwave heating leads to pyrolysis of the precursor molecules. At high temperatures, condensation and esterification occur between the hydroxyl and carboxylic acid groups on neighboring precursor molecules, followed by aromatization through aldol condensation and cycloaddition reactions. When a critical point of the concentration aromatic clusters in the reaction mixture has been reached, a burst nucleation occurs, forming N-GQDs. Triethanolamine is both a solvent and a nitrogen source in this reaction.[26]

A microwave power setting of 33% was found to result in the most controllable synthesis. A lower (10%) power setting resulted in the formation of a dilute solution of N-GQDs with a large amount of unreacted sodium citrate. It is assumed that the microwave irradiation was not powerful enough to sufficiently dehydrate the precursor citrate molecules to allow the formation of many N-GQDs. A higher (100%) power setting resulted in the formation of a solid substance, presumed to be graphene oxide, as the higher temperatures reached allowed for the agglomeration of the nanoparticles.

Varied irradiation times were tested (150 s, 165 s, 180 s and 195 s) to identify the effect the reaction time has on the

properties of the resulting GQDs. From here on, N-GQDs synthesized hydrothermally for varying reaction times will be referred to as HT1, HT2, HT3 and HT4 for reaction times 150 s, 165 s, 180 s, and 195 s, respectively. The literature reports the formation of a pale-yellow solution of the reaction mixture, indicating the formation of N-GQDs.[27] It was observed that a pale-yellow solution was formed for HT1, and the solutions darkened upon increasing the reaction time (Fig. 3). Samples were illuminated with a 395 nm UV torch upon synthesis to ensure fluorescence was present, as further proof of the GQDs formation.

Electrochemical synthesis of N-GQDs

The electrochemical synthesis of N-GQDs from graphite rods is a top-down synthetic method. The electrolyte for the reaction was a solution of sodium citrate, triethanolamine and water since utilizing the same reagents for both the hydrothermal and electrochemical GQD synthesis was likely to create comparable GQDs across synthetic methods, particularly ensuring triethanolamine is present in both reactions since a nitrogen source is required to synthesize N-GQDs. The decision was made to electrolyze the electrolyte solution before its use in the synthesis of GQDs to induce more hydroxyl ions in the solution. Typical electrochemical synthesis of GQDs employs dilute NaOH as an electrolyte due to its easy dissociation, resulting in high availability of OH^- ions. Through experimentation, it was found that dissociation of triethanolamine and sodium citrate into free OH^- ions is unlikely under the reaction conditions used, and therefore, the electrolysis of water before the reaction began introduced a sufficient quantity of ions to the electrolyte.

When a potential is applied to the graphite rod electrodes in the electrolyte, the OH^- ions oxidize on the defect sites on the surface of the graphite rod, producing oxygen, which then forces the graphite layers apart. Further ions then intercalate between the layers, widening the layer spacing further. The electric field cleaves the C=C bonds, and ultimately, the graphite rods are electrochemically exfoliated, forming GQDs.[28] This electrochemically synthesized sample will now be referred to as EC1.

Physical analysis

XRD. XRD analysis was carried out for each solution to confirm the presence of graphitization and crystallinity in the structures. The XRD patterns for all studied N-GQDs showed the expected trend with two features, d_{100} in-plane lattice spacing of graphite and d_{002} diffraction peak. The XRD graphs of samples HT1-4 displayed a diffraction peak at $2\theta = 23.89°$ due to the C (002) crystal plane index, indicative of an aromatic structure with a high degree of parallel and azimuthal orientation, thus confirming the structure is graphene. A typical XRD graph for a hydrothermally synthesized N-GQD is shown in (Fig. 4a), noting that all HT1-4 N-GQD specimens displayed XRD peaks in the same locations. The unsymmetrical nature of the peak suggests the presence of aliphatic structures doped on the surface of the N-GQDs, as was expected due to the introduction of nitrogen and oxygen-containing groups during synthesis. Furthermore, this diffraction peak ($2\theta = 23.89°$) corresponds to a d_{002} spacing of 0.37 nm. This is slightly larger than the interlayer spacing of graphite (0.334 nm). However, this increase can be attributed to the presence of functionalization on the basal plane, forcing the graphene layers further apart.[29]

The smaller peak at $2\theta = 37.34°$ corresponds to the d_{100} plane index. This represents the length of the unit cell and is equivalent to 0.24 nm, close to the d_{100} spacing in graphite (0.246 nm), further emphasizing the graphitic nature of the nanoparticles.

The XRD graph of EC1, shown in Fig. 4b, is similar, displaying a Bragg diffraction peak at $2\theta = 28.82°$, corresponding to a d_{002} spacing of 0.31 nm, slightly smaller than the interlayer spacing of graphite (0.334 nm). This decrease in the interlayer spacing compared to graphite is likely a result of curvature at the edges of the N-GQDs on EC1 due to the sp bonds, as outlined in the introduction. Since the edge-to-core ratio is extremely high for small N-GQDs, X-rays interact with a high proportion of distorted nanoparticle edges, thereby yielding a reduced d_{002} spacing.

Furthermore, the interlayer spacing of EC1 does not display an increase in interlayer spacing due to basal plane functionalization. Synthesizing GQDs using a bottom-up technique (HT GQDs) is more likely to result in extensive basal plane functionalization since smaller organic molecules must pyrolyze and stack to form the GQDs under high temperatures. In contrast, the top-down synthetic technique from graphite rods (EC1) requires that electrochemical exfoliation of high-purity graphite occurs. The layers will break apart where OH^- ions have intercalated into the graphite rod, meaning the resulting nanoparticle will have few remaining hydroxyl groups between the layers of the synthesized GQD, since if enough penetration of OH^- ions had occurred between the layers, the particle would have been electrochemically cut at this position under the influence of the applied potential. Any functionalization with oxygen-containing or amine groups is thus primarily located on the external basal plane (*i.e.* on the top and bottom of the GQD) and edges of the nanoparticle.

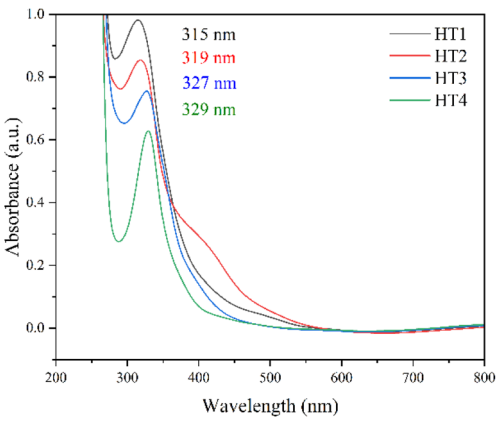

Fig. 5 Effect of the reaction time on the UV-Vis spectra of hydrothermally synthesized N-GQDs.

Table 1 Comparison of synthesized N-GQDs to published works

Sample	Synthesis time/s	Particle size/nm	Bandgap/eV
HT1	150	5	2.47
HT2	165	18	2.30
HT3	180	27	2.02
HT4	195	40	1.96
EC1	3600	6	2.58
N-GQDs derived from coal[34]	Reflux 24 h followed by N doping	5.86	2.05
N-GQDs derived from graphene oxide[35]	Hydrothermal (autoclave) 10 h	3.2	2.36
N-GQDs derived from carbon cloth[36]	Electrochemical cutting 24 h	3.1	2.83

The second peak at $2\theta = 40.07°$ (Fig. 4b) corresponds to the d_{100} plane index and is equivalent to 0.22 nm. Whilst this is, again, slightly smaller than that of graphite (0.246 nm), the value aligns with the previously reported lattice constant of nitrogen-doped graphene (0.227 nm).[30]

The variation in relative peak intensity between Fig. 4a (HT1) and Fig. 4b (EC1) was not unexpected, as the preparation method of GQDs is known to influence diffraction peak intensity. GQDs prepared by top-down methods (EC1) are known to have a more intense (100) peak than GQDs prepared *via* bottom-up methods (HT1).[31]

UV-Vis. The increase in the size of the hydrothermally synthesized nanoparticles with reaction times is supported by UV-Vis spectra (Fig. 5). The peaks between 315 and 329 nm are a result of the π–π* transition in C=C within the sp^2 region of the graphene lattice. The redshift seen in the spectra indicates a narrowing of the bandgap, as is expected upon increasing nanoparticle size[9] (eqn (1)). The increase in particle sizes can be explained as follows; the longer heating times allowed more dehydration reactions to occur, enlarging the synthesized quantum dots. The shoulder at ~410 nm in HT2 is likely due to n–π transition of oxygen or nitrogen containing functional groups.

It has previously been demonstrated that nitrogen-enriched carbonaceous quantum dots possess adsorbed anionic water clusters ($[OH(H_2O)_n]^-$) on their surface in solution,[32] which will therefore affect the bandgap of the nanoparticles due to changes in size/surface area of the particles upon their addition. Since all other structural and electrochemical testing was conducted in solution, either diluted or with an aqueous electrolyte, drying the samples to determine their concentration was not worthwhile since the absence of water clusters will alter the N-GQD structure. Instead, the absorption coefficient was estimated by diluting samples relative to each other and plotting a graph of the peak absorption coefficient against the relative concentration of each sample. The best linear fit was then plotted, and its slope was determined. The slope of this line is equal to the product of the extinction coefficient and path length. The path length for the UV-Vis measurements was 1 cm. Based on these approximated absorption coefficients, Tauc plots were graphed (Tauc plot for HT1 shown in Fig. S1). The best-fit line of the linear section of the graph was then extrapolated down to the *x*-axis, giving the value of the bandgap.

The bandgaps for HT1-4 were 2.47, 2.30, 2.02 and 1.86 eV, respectively (Table 1). These values are within the reported bandgap ranges for GQDs.[33] Furthermore, these values confirm that the redshift seen in the UV-Vis spectra is representative of a narrowing of the bandgap upon increasing particle size. This is due to a weakening of the quantum confinement effect upon increasing nanoparticle size as a larger number of atomic orbitals are involved in bonding in the particles, decreasing the distance between the empty and filled states and thus decreasing the bandgap.

The UV-Vis spectrum of the electrochemically synthesized N-GQDs (EC1) is shown in Fig. 6. The peak at 293 nm, is a result of the π–π* transition in C=C. From the Tauc plot, the bandgap for EC1 was found to be 2.58 eV. This bandgap is within the

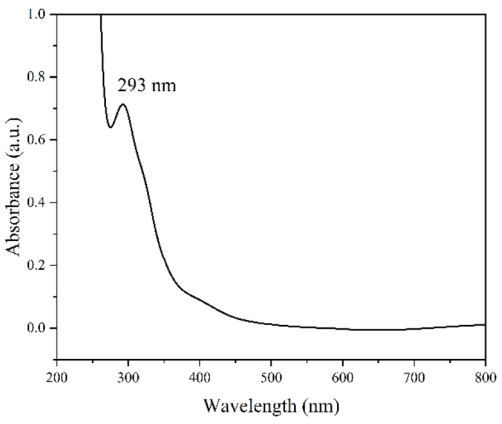

Fig. 6 UV-Vis spectrum of sample EC1. The peak at 293 nm results from C=C bonds.

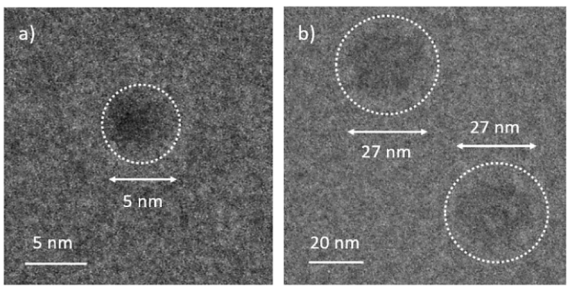

Fig. 7 TEM images of (a) HT1 and (b) HT3.

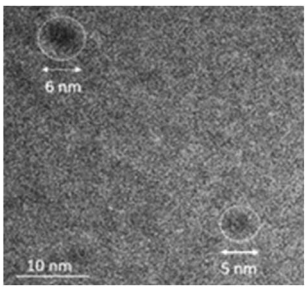

Fig. 8 TEM images of sample EC1. The sample showed increased polydispersity compared to hydrothermally synthesized N-GQD samples, with an average size of 6 nm.

expected range for N-GQDs[33] and will be discussed in relation to the UV-Vis spectra of hydrothermally synthesized N-GQDs, as shown in Table 1.

Due to the high variability of GQD bandgaps, there are no fixed bandgap values that are expected to be seen. For instance, different synthetic methods produce nanoparticles of similar sizes, but varied bandgaps (Table 1). The data from published works (Table 1) include N-GQDs synthesized both hydrothermally and electrochemically for comparison to this work.

TEM. The TEM images (Fig. 7) support the increase in the lateral dimension of the N-GQD size upon increased microwave reaction time (~5 nm for HT1, ~18 nm for HT2, ~27 nm for HT3, ~40 nm for HT4, Fig. S2 and Table 1).

The TEM image of EC1 (Fig. 8) showed that the average size of the nanoparticles was 6 nm, meaning they are comparable in size to HT1 nanoparticles and will be compared directly against them. However, some variability in the dimensions of EC1 nanoparticles compared to HT1 was observed, with diameters between 5 and 7 nm.

It should be noted that the electrochemical synthesis was less controllable than the hydrothermal synthesis; altering the reaction time did not affect the size of the electrochemically synthesized nanoparticles. For this reason, only samples HT1 and EC1 were taken forward to the next step of the study.

Raman spectra. The edge shapes of the synthesized quantum dots were confirmed by the Raman spectra shown in Fig. 9. The spectra have been fitted using a Lorentzian function. In previous papers, there has been some variability in the Raman spectra for GQDs.[37,38] In the work presented here, the authors aim to provide an in-depth analysis of the origin of the variability and its explanation with respect to the edge shapes of the nanoparticles.

The D band in GQDs originates from the intervalley double resonance processes arising from the scattering of electrons by the combination of a defect and a phonon, where the particle's edge behaves as the defect.[39] In N-GQDs, the D band is closely associated with the quantum confinement effect due to the influence of edge states. For intervalley resonance in graphene, the scattering occurs between two inequivalent points in the Brillouin zone. The orientation of the AC edges allows their associated wavevectors to connect points in the $\boldsymbol{K} + q$ region surrounding these points, however, the laser power used in this

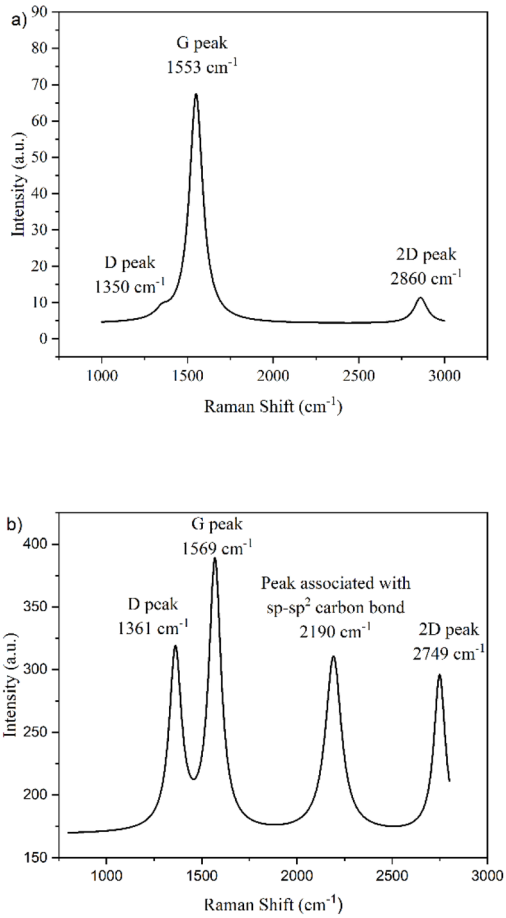

Fig. 9 Raman spectra of (a) HT1 (ZZ N-GQDs) and (b) EC1 (AC N-GQDs).

work would not have allowed this to occur for ZZ edges.[39] This results in the prominence of a D band for AC N-GQDs. For this reason, it is clear that sample HT1 contains ZZ edges, while sample EC1 contains AC edges (Fig. 1). The occurrence of a weak D band for ZZ N-GQDs (Fig. 9a) arises due to imperfections in the atomic structure of the ZZ N-GQDs, likely resulting from the presence of doped and/or functionalized groups on their edges.

The G band results from the in-plane vibrational mode of sp^2 carbon atoms. The typical G band of graphene appears at ~1580 cm^{-1}.[40] Here, the G band for HT1 (ZZ N-GQDs) appears at 1553 cm^{-1}, compared to that for EC1 (AC N-GQDs) at 1569 cm^{-1}. The G mode is polarization-dependent due to the two doubly degenerate phonon modes, longitudinal optical (LO) and in-plane transverse optical (iTO) phonons at the Brillouin zone center. However, it has previously been shown that the LO mode is only active at AC edges.[41] This allows the Kohn anomaly to occur at AC edges, whereby anomalous behavior in the dispersion of phonons is observed, leading to a redshift of the G mode, accounting for its decreased Raman shift.[41] The redshift observed in the Raman shift of ZZ N-GQDs, on the other hand, is most likely due to functionalization on the edges of the nanoparticles. The larger G peak Raman shift of the AC edges compared to the ZZ edges observed in Fig. 9 agrees with the work of Kim *et al.*[42]

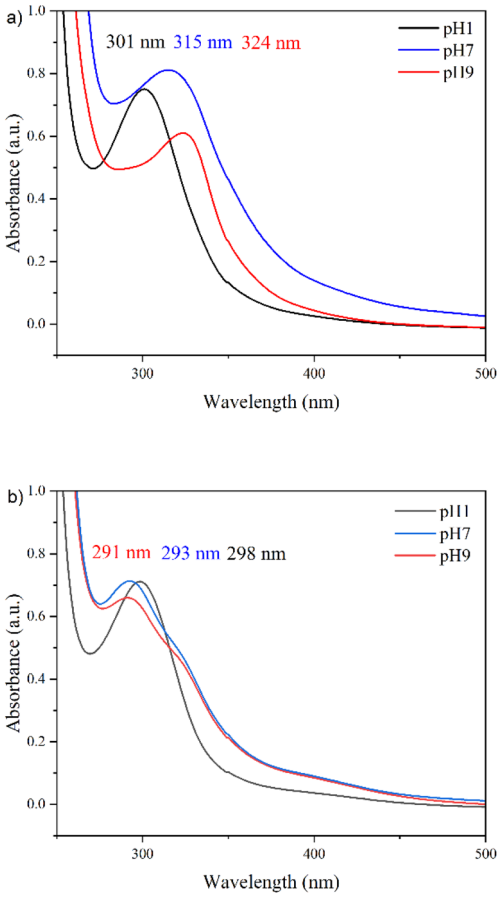

Fig. 10 Effect of the pH on UV-Vis spectra of (a) HT1 (ZZ N-GQDs) and (b) EC1 (AC N-GQDs).

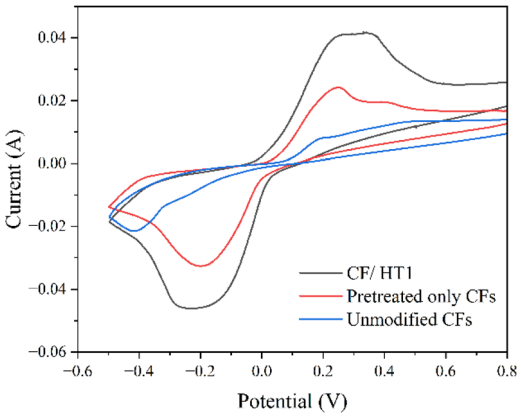

Fig. 11 Cyclic voltammograms of unmodified carbon fibers (blue), pretreated carbon fibers (red) and carbon fibers with hydrothermally synthesized (HT1) N-GQDs electrodeposited (black) in 1 M H_2SO_4 electrolyte. Scan rate was 5 mV s^{-1}.

AC edges contain triple bonds between the carbon atoms at the edges of the GQD. The peak at 2190 cm^{-1} in EC1 (AC N-GQDs) (Fig. 9b) is indicative of the effective conjugation coordinate (ECC) mode, a vibrational parameter whereby the bond length alteration parameter oscillates.[43] The ECC consists of the simultaneous stretching of the C≡C bonds and contraction of their neighboring C–C bonds, a direct consequence of translational symmetry at the edges of the lattice structure. This symmetry is satisfied by the shrinking of the C–C bonds when the two attached C≡C bonds stretch in phase, preventing the atomic displacements of the phonons, in the Brillouin zone center, from modifying the cell volume.[44] This peak therefore demonstrates the presence of sp–sp^2 carbon bonds at the edges of EC1 (AC N-GQDs), which do not exist in HT1 (ZZ N-GQDs). Suganya *et al.* similarly found a Raman band at 2198 cm^{-1} as a result of C≡C bonds.[45]

The 2D band is an overtone of the D band. The 2D band can occur without the presence of a D band since the 2D double resonance processes involve two phonons, specifically two transverse optical phonons near the ***K*** point. This differs to the D band where a defect and a phonon are required, and hence a 2D band is observed in both ZZ and AC N-GQDs. The 2D bands are low in intensity compared to the G bands, as the probability of recombination occurring before two electron-phonon scattering processes can occur, is high.[46]

pH variation. The effects of the pH on the bandgap of N-GQD samples synthesized through both methods were studied using UV-Vis spectroscopy (Fig. 10). The pH of the N-GQD solutions was adjusted with 70% nitric acid and sodium bicarbonate salt. It was found that the N-GQDs produced by hydrothermal microwave-assisted synthesis exhibit changes in their wavelength absorption with pH variation, whereas the N-GQDs produced electrochemically (EC1) display no changes in peak position.

Many reports in the literature state that the bandgap of GQDs is pH-dependent.[25] However, based on the obtained UV-Vis spectra (Fig. 10), it has been found that this is not the case for all GQDs. An explanation for this result is provided by considering the edge structure of ZZ and AC edged GQDs. ZZ GQDs contain a carbene-like double bond at their edges and possess a dangling bond that can be readily protonated or deprotonated. When ZZ GQDs are exposed to a low pH, their edges will protonate, increasing the size of the sp^2 domain and thus narrowing their bandgap (Fig. 10a). The opposite will be true for ZZ GQDs suspended in basic media, whereby their edges will deprotonate, decreasing the sp^2 domain and hence, widening their bandgap.

GQDs with AC edges are only slightly influenced by variations in the pH of their surrounding environment (Fig. 10b). This is because armchair-edged GQDs have a carbyne-like triple bond. Hence, have no free bonds available to protonate/deprotonate. The slight bandgap variations likely result from some basal plane functionalization on defect sites due to the additional oxygen-containing groups available upon acid/base addition. Therefore, these results support the Raman results in demonstrating that hydrothermally synthesized N-GQDs contain ZZ edges, while electrochemically synthesized N-GQDs contain only AC edges (Fig. 1).[47]

Furthermore, the synthesized EC1 N-GQDs are of a similar size to HT1, the ZZ N-GQDs with the smallest lateral

Table 2 Comparison of electrodes modified by GQDs. Initial capacitance is the specific capacitance of the electrode before GQD addition, final capacitance is the specific capacitance after their addition

Electrode material	Scan rate/current density	Initial capacitance/F g^{-1}	Final capacitance/F g^{-1}	Reference
CF/HT1	5 mV s^{-1}	16	60	This work
GQDs/3D graphene	1.25 A g^{-1}	136	268	51
Carbon nanofibers/GQDs	0.5 A g^{-1}	252	332	53
GQDs/activated carbon	1 A g^{-1}	Not available	388	54
S, N-GQDs/PANI	0.5 A g^{-1}	177	645	55

dimensions, and it is known that AC N-GQDs display a larger bandgap than ZZ N-GQDs of the same size (Table 1). This is a direct consequence of the dispersionless edge states present in ZZ N-GQDs that are not observed in AC N-GQDs.[9] The degenerate zero energy edge states in the ZZ N-GQDs follow Hund's rule and allow additional energy level transitions that do not occur in AC GQDs. The bandgap difference between ZZ and AC GQDs is more evident for smaller GQDs as the ratio of edge atoms to central atoms is increased.

The implications of the bandgap changes upon pH variation are of extreme significance to the electrolyte selection of any electrochemical device containing ZZ N-GQDs. If an acidic electrolyte is selected, it will narrow the particles' bandgap, while a basic electrolyte will widen it. For this reason, small ZZ N-GQDs combined with an acidic electrolyte will provide the greatest increase in specific capacity of supercapacitors. It has previously been reported by Liu *et al.*[48] that smaller GQDs display higher rate capability and faster frequency response times than larger GQDs. Smaller nanoparticles result in shorter ion diffusion distances and, therefore, shorter ion diffusion times. Smaller N-GQDs also possess a higher surface area to volume ratio, increasing the surface area of the electrodes to a greater extent than larger nanoparticles, providing a greater area upon which the electrical double-layer can form. Furthermore, smaller N-GQDs contain the largest ratio of edge to core, increasing the benefit of the edge shapes in each nanoparticle. Although smaller nanoparticle size results in a wider band gap, which can negatively affect specific capacitance, the doping of GQDs with nitrogen narrows the bandgap and provides a faradaic energy storage component to the specific capacitance. Therefore, it mitigates some of the adverse effects on capacitance. These factors, combined with further narrowing of the bandgap due to the acidic electrolyte, provide ideal conditions for maximizing energy storage in the ZZ N-GQDs.

Effect of the edge type of the N-GQDs on the electrochemical performance of CF electrodes

GQDs have previously been integrated into various electrode materials for supercapacitor applications, including metal hydroxides,[49] disulfides,[50] and various carbon-based materials.[51] In all cases, the addition of GQDs enhances the supercapacitor electrodes performance, most notably by increasing the specific capacitance. To demonstrate the benefits of depositing N-GQDs and establish the influence of the edge shapes of the GQDs on the performance, carbon fiber electrodes were used. Carbon fibers were chosen due to their inherently low specific capacitance in the unmodified state, allowing the improvements arising from N-GQD incorporation to be more clearly distinguished.

Cyclic voltammetry (CV) was carried out on carbon fibers (CFs) with N-GQDs electrodeposited for various times (10 min, 20 min, 30 min, 40 min, 50 min, and 60 min). The specific capacitances of electrodes with each deposition time were calculated from the CV curves. It was found that the ideal deposition time was 30 minutes; shorter times resulted in fewer deposited N-GQDs and therefore the specific capacitances of the doped carbon fiber electrodes were lower, while at longer deposition times the deposited N-GQDs began to agglomerate on the surface of the fibers, lowering the surface area of the N-GQDs and consequently also reducing the capacitance (cyclic voltammograms for 10 min, 30 min and 60 min shown in Fig. S3).

The voltammogram of the CFs modified with HT1 N-GQDs displayed (Fig. 11) an expected increase in redox peaks compared to unmodified and pre-treated carbon fibers due to the faradaic groups present on the N-GQDs. The specific capacitances of the unmodified, pretreated-only, and CFs with electrodeposited N-GQDs were 16, 37 and 60 F g^{-1}, respectively, showing a 275% increase in the specific capacitance for HT1 modified CFs. It is worth noting that the increase in specific capacitance for the pretreated-only CFs is due to pseudocapacitive reactions arising from the addition of oxygen groups to their surfaces during ultrasonication in concentrated nitric acid. Some redox peaks are also visible on the voltammogram of unmodified carbon fibers. It has previously been demonstrated by Gulyas *et al.*[52] that neat carbon fibers contain faradaic groups on their surface, including phenolic OH, carboxyl, carbonyl and/or adsorbed water, which would contribute to redox reactions.

The specific capacitance of CF/HT1 has been compared with other GQD-modified electrodes in Table 2, where all electrodes were tested using 1 M H_2SO_4 as the electrolyte. A direct comparison of different GQD-based electrodes is challenging due to the many variables that influence electrochemical performance, *e.g.*, synthesis route, size distribution, and GQD functionalization. Nonetheless, in all reported cases, the incorporation of GQDs resulted in at least a 60% increase in specific capacitance.

The specific capacitance of the CFs doped with HT1 (ZZ N-GQDs), calculated from CV curves in 1 M H_2SO_4 electrolyte, was 60 F g^{-1}, compared to 31 F g^{-1} for CFs doped with EC1 (AC

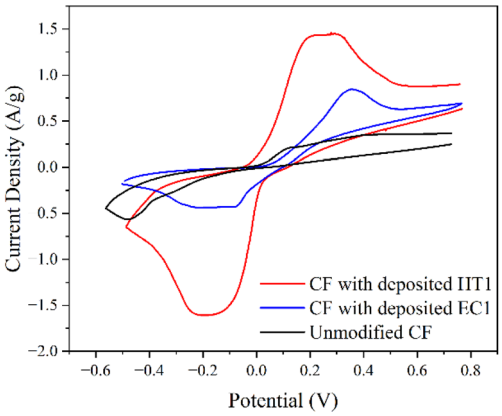

Fig. 12 Cyclic voltammograms at 5 mV s^{-1} of carbon fibers with electrodeposited HT1 (black) and EC1 (red) N-GQDs and unmodified carbon fibers (blue) in 1 M H_2SO_4 electrolyte.

N-GQDs). To note, the bandgap of the ZZ N-GQDs during electrochemical testing was 1.98 eV due to the use of the acidic electrolyte (calculated using the Tauc method). Evidently, this is smaller than the measured bandgap of 2.47 eV of the same nanoparticles in a neutral environment.

The dangling bonds present at the edges of ZZ N-GQDs increase their affinity for edge site doping, allowing faradaic groups to attach and thus improving their pseudocapacitive storage capability. The cyclic voltammograms for carbon fiber electrodes with HT1 and EC1 deposited on their surfaces are shown in Fig. 12, demonstrating the increased quantity of redox reactions for HT1 compared to EC1.

The redox capabilities demonstrated by EC1 (AC N-GQDs), albeit somewhat limited, originate from the functionalization of their edges with oxygen and amine groups, alongside nitrogen doping. Defects were induced by heating the graphite rods during synthesis, which allowed nitrogen doping to occur at these defect sites during electrodeposition. Moreover, the electrochemical cleaving of carbon bonds during synthesis created edge defect sites for functionalization on the N-GQD edges. This introduced faradaic groups to the nanoparticles, allowing some pseudocapacitive charge storage to occur. Despite the presence of the defects, the functionalization of the AC N-GQDs was more limited than HT1 (ZZ N-GQDs) due to the lack of dangling bonds.

The specific capacitance of carbon fibers with AC N-GQDs deposited (31 F g^{-1}) is lower than that of pretreated-only CFs (37 F g^{-1}) (Table 3). This can be explained by the faradaic processes which take place on the electrodes during the measurements. The oxygen-containing functional groups that are introduced to carbon fibers through pre-treatment are able to participate in redox reactions. However, these active sites are effectively 'used up' during N-GQD deposition (N-GQDs bond to the oxygen groups), and the deposited AC N-GQDs have fewer available redox sites than the oxygenated CFs, resulting in a lower specific capacitance.

Four cyclic voltammetry cycles were performed at 5 mV s^{-1} for both CF/HT1 and CF/EC1 electrodes. No change in specific capacitance was observed across cycles, indicating good electrochemical stability under the tested conditions. However, since this study serves as a proof of concept, more extensive experiments are required to evaluate the long-term stability of these electrodes. Such long-duration cycling tests were beyond the scope of this work. Future studies will focus on assessing degradation mechanisms and the retention of performance over time.

Table 3 Specific capacitances obtained from cyclic voltammetry for carbon fiber-based electrodes

Electrode	Specific capacitance (F g^{-1})
Unmodified carbon fibers	16
Pretreated only carbon fibers	37
Carbon fibers with HT1 (ZZ N-GQDs) deposited	60
Carbon fibers with EC1 (AC N-GQDs) deposited	31

The Nyquist plots (recorded between 50 mHz and 10 kHz) for the CF electrodes modified with N-GQDs (Fig. S4) exhibit semicircles, which are characteristic of charge-transfer processes or faradaic reactions. The internal resistance of the system incorporating ZZ N-GQDs was found to be 22.13 Ω, compared with 44.71 Ω for electrodes containing AC N-GQDs. This reduction in resistance is attributed to the higher density of faradaic functional groups present on the ZZ N-GQDs. The equivalent circuit used for fitting, shown in the inset of Fig. S4, corresponds to a classic Randles circuit. As expected, electron-transfer kinetics dominate over diffusive processes in these systems due to the pseudocapacitive behavior introduced by the N-GQDs.

Quantum capacitance

Quantum capacitance is a factor often overlooked when selecting electrode materials for supercapacitors. Increasing the quantum capacitance of an electrode material is known to increase the energy density of the supercapacitor.[56] This is due to the close relationship (direct proportionality) between quantum capacitance and density of states of the electrode (eqn (3)). An increased number of states for electron occupation results in increased energy storage.

From here on, the electrodes will be referred to as ZZCF (carbon fibers with HT1 electrodeposited) and ACCF (carbon fibers with EC1 electrodeposited). The double layer capacitance (C_{dl}) values were found to be 0.65 F g^{-1} and 0.49 F g^{-1} for ZZCF and ACCF, respectively. The higher C_{dl} value observed for the ZZCF electrodes can be attributed to the fact that EDL capacitance increases with increasing accessible material surface area.

The C_{dl} values were subsequently used to calculate the quantum capacitance (C_q). C_{total} values were obtained from the EIS plots described in the experimental section, but were conducted at different potentials, as is explained below, and the C_q values were calculated using eqn (2). Capacitance values are frequency-dependent due to localized dielectric polarization

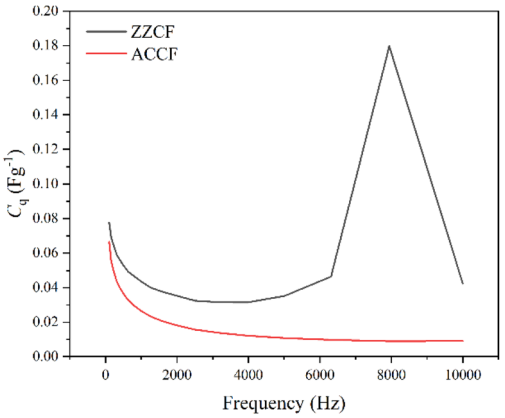

Fig. 13 Quantum capacitance profile for ZZCF and ACCF samples. The peak in the ZZCF profile is a van-Hove singularity, indicative of the presence of edge states.

effects. The quantum capacitance was therefore calculated for the frequency range 10 kHz to 100 Hz.

To avoid errors relating to depletion and accumulation layers between the electrodes and the electrolyte, Mott–Schottky analysis was used to determine the flatband potential (V_{fb}) for the ZZCF and ACCF electrodes in the half-cell configuration. This was necessary to determine a potential at which to produce EIS plots for each electrode from which the values of C_q were determined to ensure that the charge carriers at the electrode–electrolyte interface were in similar states for both electrodes, and differences in quantum capacitance measurements weren't a result of surface states. The N-GQD-modified electrodes were determined to be n-type based on the positive linear slope displayed in the Mott–Schottky graphs (Fig. S5). Pristine GQDs have been found to be p-type semiconductors.[57] However, the n-type nature of the N-GQDs can be attributed to the electron-donating effects of the doped nitrogen atoms. The flatband potentials were determined to be 0.21 and 0.29 V *vs.* Ag/AgCl standard reference electrode for ACCF and ZZCF, respectively. These values align with that for nitrogen-doped graphene, where a flat band was shown to appear at 0.35 V.[58]

EIS plots were obtained at the flat band potential for each electrode. The lowest frequency was selected to be 100 Hz as the N-GQDs displayed electric field reversal at lower frequencies, resulting from nonsynchronicity between the phases of the scan and internal accumulated carrier state in the N-GQDs.[59] Fig. 13 displays the quantum capacitance variation over the given range for both electrodes. It can be seen that C_q is larger for ZZCF than ACCF for all frequencies at its flatband potential.

To note, quantum capacitance is directly proportional to the square root of the DOS, and the overall shape of the quantum capacitance profile is therefore the same as the shape of the DOS profile for the electrodes at these frequencies at the flatband potentials. A van-Hove singularity can be seen in the profile for ZZCF at ~8000 Hz and is indicative of the presence of edge states.[60] The singularity is only present for ZZCF since ZZ N-GQDs display dispersionless edge states, while AC N-GQDs do not.

The increased quantum capacitance of ZZ N-GQDs compared to AC N-GQDs in the studied frequency range, shown in Fig. 13, further explains their increased performance in energy storage devices.

Conclusions

Graphene quantum dots (GQDs), with their high surface-to-volume ratio, tunable bandgaps, and exceptional stability, are promising materials for the next-generation energy storage systems. Yet, the influence of edge configuration (zigzag (ZZ) *versus* armchair (AC)) on electrochemical performance has remained largely unexplored, leaving a critical gap in understanding. This study addresses that gap by synthesizing nitrogen-doped GQDs (N-GQDs) with controlled ZZ and AC edges *via* hydrothermal and electrochemical methods, followed by their electrodeposition onto carbon fiber electrodes. Comprehensive characterization using XRD, TEM, UV-Vis, Raman spectroscopy, and electrochemical techniques (CV, EIS) revealed that, for GQDs of similar sizes, ZZ-edged N-GQDs consistently outperform AC-edged counterparts in capacitance, encompassing double-layer, pseudocapacitance, and quantum contributions. This superior performance stems from the higher density of states associated with dispersionless edge states unique to ZZ configurations.

Moreover, we demonstrate that environmental pH selectively modulates the bandgap of ZZ-edged N-GQDs (unlike that of AC-edged N-GQDs), offering a practical strategy for electrolyte selection and fine-tuning device properties. These findings underline the importance of 'edge engineering' in optimizing energy storage performance and demonstrate that precise nanoparticle design is achievable through controlled synthesis.

Beyond identifying a cost-effective route to synthesize stable ZZ-edged GQD fabrication of desired nanoparticle size, this work establishes a fundamental baseline for targeted device development, enabling high-performance supercapacitors and batteries. Furthermore, the demonstrated edge-dependent electronic behavior opens new opportunities for broader applications in optoelectronics, including solar cells, LEDs, lasers, and photodetectors, where bandgap control ('bandgap engineering') is critical.

By linking synthesis methods, edge structure, energy bandgap and electrochemical behavior, this study provides practical insights for the development of sustainable, high-efficiency energy storage devices and opens innovation routes in nanomaterial design.

Experimental

Materials

Triethanolamine (85%) (TEA, $C_6H_{15}NO_3$), trisodium citrate ($Na_3C_6H_5O_7 \cdot 2H_2O$) and sodium hydrogen carbonate ($NaHCO_3$) were purchased from Mistral Industrial Chemicals, Ltd NI. Nitric acid (70%) (HNO_3) was purchased from Thermo Fisher Scientific, Ltd. Sulfuric acid (1 M) (H_2SO_4) was purchased from Rapid Electronics, Ltd. Isopropyl alcohol (IPA, $(CH_3)_2CHOH$) was purchased from Sigma-Aldrich. All chemicals were of research grade. Carbon fibres (plain weave Pyrofil TR 30S 3K, 210 gsm, 300 μm thickness) were obtained from Easy

Composites. Graphite rods (70 mm length, 3 mm diameter, 99.9% purity) were obtained from Redoxme and were HP-III grade. A platinum rod counter electrode (85 mm length, 6 mm diameter, platinum content 50 g m^{-2} coated on type 2 titanium) was obtained from Spa Plating, Ltd. An Ag/AgCl reference electrode (aqueous, filled with 3 M saturated KCl) was obtained from Ossila, Ltd. A PTFE copper electrode holder (10 × 10 mm copper plate conductive substrate, PTFE body and gold-plated copper rod terminal) and an electrochemical cell (50 ml, borosilicate glass, PTFE lid) were obtained from Stonylab. All chemicals were used as received.

Hydrothermal synthesis of nitrogen-doped GQDs

Nitrogen-doped GQDs (N-GQDs) were synthesized using a microwave-assisted hydrothermal method, similar to that published by Ren *et al.*[27] 2 g of sodium citrate were mixed with 12 cm^3 of triethanolamine. The solution was stirred for 1 hour and was then placed in a domestic microwave oven (COMFEE, 700 W) at 33% power for times varying from 150 s to 195 s.

Electrochemical synthesis of nitrogen-doped GQDs

N-GQDs were synthesized by the electrochemical exfoliation of graphite rods. A modified version of the work by Bahadur *et al.*[28] was used. Graphite rods were first heated at 200 °C in an oven for 30 minutes, then manually exfoliated using an abrasive pad (grit number 150) to remove the external oxide layer formed upon cooling and washed with deionized water to remove any larger surface particles. 2 g of sodium citrate, 12 cm^3 triethanolamine and 25 cm^3 deionized water were added to an electrochemical cell. The solution was allowed to electrolyze for 20 minutes using platinum and nickel electrodes by applying chronoamperometry at 10 V (using VersaSTAT 3 Potentiostat Galvanostat). The graphite rods were then used as both the working and the counter electrodes and chronoamperometry at 10 V was applied for 1 hour. The resulting solution was filtered through a 450 nm syringe filter to remove any graphite particles.

Physical characterization of GQDs

UV-Vis spectra of the N-GQD samples were measured using a UV-Vis spectrophotometer (Shimadzu UV-Vis UV 1800, 190–1100 nm scan range). The samples synthesized hydrothermally were diluted in a 1 : 50 volume ratio with deionized water. In contrast, the electrochemically synthesized GQDs were diluted in a 1 : 20 ratio with deionized water to ensure all samples had a similar peak absorbance value. Samples were placed in a 3.5 ml UV quartz cuvette with a 1 cm path length and measured in a range of 190–700 nm.

Lateral size measurements of the GQDs were recorded using a transmission electron microscope (TEM) (JEOL JEM-2100). Hydrothermally synthesized samples were diluted in a 1 : 4 ratio with IPA, while electrochemically synthesized samples were diluted in a 1 : 2 ratio with IPA. Samples were drop casted (2 drops) onto 200 mesh carbon-coated copper grids, allowed to dry, and viewed under the TEM with an acceleration voltage of 200 keV at a resolution of 5 nm. More than 10 GQDs were imaged per sample using TEM, all displaying similar lateral sizes.

Crystallographic measurements of the GQDs were taken using X-ray diffraction (XRD) analysis (Bruker D8 Advance) with monochromatic CuKα radiation. Samples were drop-casted onto a glass substrate and allowed to dry. Curves were obtained between 10 and 90° (2θ) at 40 kV and 35 mA with a 0.02° per s scan rate.

Raman spectra were obtained using a confocal Raman microscope (Horiba LabRAM HR Evolution) with an excitation wavelength of 532 nm. Samples were spray-coated onto silicon wafers and allowed to dry. Spectra were obtained between 100 and 300 cm^{-1} with an acquisition time of 800 s.

Deposition of GQDs on carbon fiber electrodes

Electrophoretic deposition was used to attach N-GQDs to carbon fibers.[61] Carbon fibers were first prepared by ultrasonicating 0.5 g carbon fibers with 0.5 cm^3 of concentrated nitric acid for 10 minutes to increase hydrophilicity and remove sizing, followed by twice ultrasonicating in 0.5 cm^3 of deionized water for 10 minutes. The washed carbon fibers were screwed into a copper electrode holder. The carbon fibers were used as the working electrode and a platinum rod was used as the counter electrode in a 2-electrode half-cell with an N-GQD solution as the electrolyte (hydrothermally synthesized N-GQDs were diluted in a 1 : 2 ratio with deionized water, while electrochemically synthesized N-GQDs were used as made since the solution was synthesized using deionized water). 10 V was applied to the cell using a DC power supply (Keithley 2200) for times between 10 min and 1 hour. The modified carbon fibers were removed from the cell and rinsed with deionized water for further testing.

Electrochemical characterization

Electrochemical measurements were carried out in a 3-electrode half-cell configuration. Carbon fibers held in a copper electrode holder were used as the working electrode, a platinum rod was used as a counter electrode and an aqueous Ag/AgCl electrode was used as the reference. The copper electrode holder was not submerged in the electrolyte and therefore did not influence the results. The electrolyte used was 1 M H_2SO_4. Cyclic voltammetry, electrical impedance spectroscopy and open cell voltage, and Mott–Schottky were all measured using a potentiostat (VersaSTAT 3 Potentiostat Galvanostat).

Cyclic voltammetry was performed to confirm the presence of N-GQDs on the surface of the carbon fibers after electrodeposition. Scans were taken at 5 mV s^{-1} scan rate in a voltage window of −0.5 to 0.8 V with 1 M H_2SO_4 as the electrolyte and each scan was taken 5 times.

Electrochemical measurements were conducted on unmodified and modified carbon fiber electrodes. Carbon fibres with deposited N-GQDs synthesized through hydrothermal and electrochemical methods were tested. The double layer capacitance was deconvoluted from the total capacitance by calculating the values separately from pseudocapacitive and quantum capacitive contributions for each electrode by

following a method by Morales and Risch.[62] This method involves obtaining cyclic voltammograms between −0.5 V and 1.2 V at slow scan rates (1–10 mV s^{-1}) with a 1 M H_2SO_4 electrolyte to determine the voltage range in which redox reactions do not occur. Voltammograms at higher scan rates (0.5–1 V s^{-1}) limited to a voltage range of 0–0.3 V were then produced to view the purely double layer contribution to capacitance (Fig. S6). iR errors (ohmic drop) were determined from the EIS Bode plot (not shown) and the voltammograms were adjusted to negate these. The contributions of unmodified carbon fiber electrodes to the capacitance measurements were eliminated from the voltammograms, so all results are reflective of only the GQDs. Next, the open circuit potentials were obtained (*via* OCP measurement), graphs were plotted of current against scan rate for currents at the open circuit potential, and the best fit lines were determined. The best-fit lines were found to be power functions, and their gradients are the C_{dl} for each electrode. Nyquist plots were recorded at a frequency range of 10 kHz to 50 mHz at 10 points per decade with an AC amplitude of 10 mV RMS and a DC potential of 0.2 V.

Mott–Schottky analysis was conducted between −0.5 and 0.8 V at 100 Hz using EIS setup. Flat band potential can be obtained from Mott–Schottky analysis by extrapolating a linear line of best fit to the *x*-axis.

Author contributions

GG: conceptualization, methodology, investigation, formal analysis and writing original draft; NS: supervision, writing – review and editing; resources; DZ, EH: supervision, writing – review and editing; KC: resources; writing – review and editing; MPP investigation.

Conflicts of interest

There are no conflicts to declare.

Data availability

Data for this article, including raw and processed datasets, is available in the Durham University Collections at https://doi.org/10.15128/r22n49t1726. Further data is supporting this article is provided in the supplementary information (SI). The supporting data has been provided as part of the supplementary information. Supplementary information: Fig. S1–S6, bandgap calculations, TEM images of the GQDs and electrochemical performance of the GQDs and supercapacitors on their basis. See DOI: https://doi.org/10.1039/d5ta09677d.

Acknowledgements

This work was supported by the Engineering and Physical Sciences Research Council [grant EP/W524426/1; DTP 2224 Durham University]. The authors thankfully acknowledge Leon Bowen and the G. J. Russell Electron Microscopy Facility for the support and use of the TEM.

References

1 K. Detka and K. Górecki, *Energies*, 2023, **16**, 5034.
2 A. Gaurav, A. Jain and S. K. Tripathi, *Review on Fluorescent Carbon/Graphene Quantum Dots: Promising Material for Energy Storage and Next-Generation Light-Emitting Diodes*, MDPI, 2022, vol. 15, p. 7888.
3 P. Kun, B. Fulop, G. Dobrik, P. Nemes-Incze, I. E. Lukacs, S. Csonka, C. Hwang and L. Tapaszto, *2D Mater. Appl.*, 2020, **4**, 43.
4 S. A. Ansari, *Nanomaterials*, 2022, **12**, 3814.
5 A. V. Vorontsov and E. V. Tretyakov, *Phys. Chem. Chem. Phys.*, 2018, **20**, 14740–14752.
6 D. Torres, J. L. Pinilla, E. M. Gálvez and I. Suelves, *RSC Adv.*, 2016, **6**, 48504–48514.
7 Z. Huang, J. Qu, X. Peng, W. Liu, K. Zhang, X. Wei and J. Zhong, *Phys. Status Solidi RRL*, 2014, **8**, 436–440.
8 M. H. M. Facure, R. Schneider, L. A. Mercante and D. S. Correa, *Environ. Sci. Nano*, 2020, **7**, 3710–3734.
9 S. A. Oliaei Motlagh and V. Apalkov, *Phys. Rev. B*, 2021, **104**, 045421.
10 L. Brey and H. A. Fertig, *Phys. Rev. B:Condens. Matter Mater. Phys.*, 2006, **73**, 1–6.
11 B. Bera, A. Chakraborty, T. Kar, P. Leuaa and M. Neergat, *J. Phys. Chem. C*, 2017, **121**, 20850–20856.
12 Y. Hanlumyuang and P. Sharma, *Jom*, 2014, **66**, 660–663.
13 Q. Xu, G. Yang, X. Fan and W. Zheng, *ACS Omega*, 2019, **4**, 13209–13217.
14 J. Zhu, A. S. Childress, M. Karakaya, S. Dandeliya, A. Srivastava, Y. Lin, A. M. Rao and R. Podila, *Adv. Mater.*, 2016, **28**, 7185–7192.
15 M. Zhang, W. Liu, R. Liang, R. Tjandra and A. Yu, *Sustain. Energy Fuels*, 2019, **3**, 2499–2508.
16 M. H. Akmal, M. Yari Kalashgrani, S. M. Mousavi and W. H. Chiang, *Nanotechnology*, 2025, **36**, 425001.
17 H. Wang, C. Wang, B. Dang, Y. Xiong, C. Jin, Q. Sun and M. Xu, *ChemElectroChem*, 2018, **5**, 2367–2375.
18 L. Sun, L. Wang, C. Tian, T. Tan, Y. Xie, K. Shi, M. Li and H. Fu, *RSC Adv.*, 2012, **2**, 4498–4506.
19 X. Feng, Y. Bai, M. Liu, Y. Li, H. Yang, X. Wang and C. Wu, *Energy Environ. Sci.*, 2021, **14**, 2036–2089.
20 Z. Zeng, S. Chen, T. T. Y. Tan and F. X. Xiao, *Catal. Today*, 2018, **315**, 171–183.
21 P. Wagner, C. Ewels, J. Adjizian, L. Magaud, P. Pochet, S. Roche, A. Lopez-bezanilla, V. Ivanovskaya, A. Yaya, M. Rayson, P. Briddon and B. Humbert, *J. Phys. Chem. C*, 2013, **117**(50), 26790–26796.
22 H. Abdelsalam, H. Elhaes, M. A. Ibrahim and A. Shams, *Sci. Rep.*, 2023, **13**, 21649.
23 A. Sheely, B. Gifford, S. Tretiak and A. Bishop, *J. Phys. Chem. C*, 2021, **125**, 9244–9252.
24 S. Zhang, L. Sui, H. Dong, W. He, L. Dong and L. Yu, *ACS Appl. Mater. Interfaces*, 2018, **10**, 12983–12991.
25 M. Aghelifar and S. Kimiagar, *Phys. Chem. Res.*, 2018, **6**, 237–250.

26 J. P. Naik, P. Sutradhar and M. Saha, *J. Nanostruct. Chem.*, 2017, **7**, 85–89.
27 Q. Ren, L. Ga and J. Ai, *ACS Omega*, 2019, **4**, 15842–15848.
28 S. Ahirwar, S. Mallick and D. Bahadur, *ACS Omega*, 2017, **2**, 8343–8353.
29 B. Zheng, Y. Chen, P. Li, Z. Wang, B. Cao, F. Qi, J. Liu, Z. Qiu and W. Zhang, *Nanophotonics*, 2017, **6**, 259–267.
30 Y. H. Hung, D. Dutta, C. J. Tseng, J. K. Chang, A. J. Bhattacharyya and C. Y. Su, *J. Phys. Chem. C*, 2019, **123**, 22202–22211.
31 M. J. Im, J. Il Kim, S. K. Hyeong, B. J. Moon and S. Bae, *Small*, 2023, **19**, 2304497.
32 M. Wiśniewski, *Int. J. Mol. Sci.*, 2022, **23**, 14292.
33 P. Rani, R. Dalal, S. Srivastava and K. Tankeshwar, *Phys. Chem. Chem. Phys.*, 2022, **18**, 26232–26240.
34 Y. Yan, J. Chen, N. Li, J. Tian, K. Li, J. Jiang, J. Liu, Q. Tian and P. Chen, *ACS Nano*, 2018, **12**, 3523–3532.
35 W. I. W. Omar, C. F. Soon, M. K. Ahmad and M. Shimomura, *Energy Environ.*, 2021, **32**, 1170–1182.
36 F. Yang, W. Bao, T. Liu, B. Zhang, S. Huang, W. Yang, Y. Li, N. Li, C. Wang, C. Pan and Y. Li, *Microchim. Acta*, 2020, **187**, 322.
37 Y. Li, Y. Zhao, H. Cheng, Y. Hu, G. Shi, L. Dai and L. Qu, *J. Am. Chem. Soc.*, 2012, **134**, 15–18.
38 E. Dervishi, Z. Ji, H. Htoon, M. Sykora and S. K. Doorn, *Nanoscale*, 2019, **11**, 16571–16581.
39 L. G. Cançado, M. A. Pimenta, B. R. A. Neves, M. S. S. Dantas and A. Jorio, *Phys. Rev. Lett.*, 2004, **93**, 5–8.
40 F. T. Johra, J. W. Lee and W. G. Jung, *J. Ind. Eng. Chem.*, 2014, **20**, 2883–2887.
41 C. Cong, T. Yu and H. Wang, *ACS Nano*, 2010, **4**, 3175–3180.
42 J. Kim, N. Lee, Y. H. Min, S. Noh, N. K. Kim, S. Jung, M. Joo and Y. Yamada, *ACS Omega*, 2018, **3**, 17789–17796.
43 P. Serafini, A. Milani, M. Tommasini, C. E. Bottani and C. S. Casari, *Carbon*, 2021, **180**, 265–273.
44 P. Serafini, A. Milani, M. Tommasini, C. Castiglioni, D. M. Proserpio, C. E. Bottani and C. S. Casari, *Phys. Chem. Chem. Phys.*, 2022, **24**, 10524–10536.
45 G. Suganya, M. Arivanandhan and G. Kalpana, *Diam. Relat. Mater.*, 2025, **151**, 111798.
46 V. Zólyomi, J. Koltai and J. Kürti, *Phys. Status Solidi B*, 2011, **248**, 2435–2444.
47 M. H. M. Facure, R. Schneider, L. A. Mercante and D. S. Correa, *Environ. Sci. Nano*, 2020, **7**, 3710–3734.
48 Y. Liu, R. Wang, J. Lang and X. Yan, *Phys. Chem. Chem. Phys.*, 2015, **17**, 14028–14035.
49 H. Jia, Y. Cai, J. Lin, H. Liang, J. Qi, J. Cao, J. Feng and W. D. Fei, *Adv. Sci.*, 2018, **5**, 1–10.
50 O. Sangabathula and C. S. Sharma, *Mater. Adv.*, 2020, **1**, 2763–2772.
51 Q. Chen, Y. Hu, C. Hu, H. Cheng, Z. Zhang, H. Shao and L. Qu, *Phys. Chem. Chem. Phys.*, 2014, **16**, 19307–19313.
52 J. Gulyas, E. Foldes, A. Lazar and B. Pukanszky, *Composites, Part A*, 2001, **32**, 353–360.
53 R. Zhang, W. Shen, M. Zhong, J. Zhang and S. Guo, *J. Phys. Chem. C*, 2021, **125**, 143–151.
54 Y. Qing, Y. Jiang, H. Lin, L. Wang, A. Liu, Y. Cao, R. Sheng, Y. Guo, C. Fan, S. Zhang, D. Jia and Z. Fan, *J. Mater. Chem. A*, 2019, **7**, 6021–6027.
55 H. Kuzhandaivel, S. Manickam, S. K. Balasingam, M. C. Franklin, H. J. Kim and K. S. Nallathambi, *New J. Chem.*, 2021, **45**, 4101–4110.
56 S. Kumar, E. Majhi, A. S. Deshpande and M. Khandelwal, *Carbon Trends*, 2024, **16**, 100385.
57 K. A. Tsai, P. Y. Hsieh, T. H. Lai, C. W. Tsao, H. Pan, Y. G. Lin and Y. J. Hsu, *ACS Appl. Energy Mater.*, 2020, **3**, 5322–5332.
58 M. M. Mohamed, M. A. Mousa, M. Khairy and A. A. Amer, *ACS Omega*, 2018, **3**(2), 1801–1814.
59 M. Guan, L. Niu, Y. Zhang, X. Liu, Y. Li and Y. Zeng, *RSC Adv.*, 2017, **7**, 50598–50602.
60 S. Pratap, S. Kumar and R. P. Singh, *Front. Phys.*, 2022, **10**, 1–12.
61 R. Tjandra, W. Liu, M. Zhang and A. Yu, *J. Power Sources*, 2019, **438**, 227009.
62 D. M. Morales and M. Risch, *JPhys Energy*, 2021, **3**, 034013.

